ARL-TR-8420 • JULY 2018

US Army Research Laboratory

# Examining the Correlation between the Peak Tensile Stress and Free Surface Velocity Measurements for Spall

by Richard Becker and Kyle Callaghan

## NOTICES

### Disclaimers

The findings in this report are not to be construed as an official Department of the Army position unless so designated by other authorized documents.

Citation of manufacturer's or trade names does not constitute an official endorsement or approval of the use thereof.

Destroy this report when it is no longer needed. Do not return it to the originator.

ARL-TR-8420 ● JULY 2018

US Army Research Laboratory

# Examining the Correlation between the Peak Tensile Stress and Free Surface Velocity Measurements for Spall

**by Richard Becker**
***Weapons and Materials Research Directorate, ARL***

**Kyle Callaghan**
***Academy of Applied Science, 24 Warren St, Concord, NH***
***Currently: University of Maryland***

# REPORT DOCUMENTATION PAGE

*Form Approved*
*OMB No. 0704-0188*



**PLEASE DO NOT RETURN YOUR FORM TO THE ABOVE ADDRESS.**

| 1. REPORT DATE *(DD-MM-YYYY)* | 2. REPORT TYPE | 3. DATES COVERED (From - To) |
|---|---|---|
| July 2018 | Technical Report | August 2017–March 2018 |

**4. TITLE AND SUBTITLE**
Examining the Correlation between the Peak Tensile Stress and Free Surface Velocity Measurements for Spall

**5a. CONTRACT NUMBER**

**5b. GRANT NUMBER**

**5c. PROGRAM ELEMENT NUMBER**

**6. AUTHOR(S)**
Richard Becker and Kyle Callaghan

**5d. PROJECT NUMBER**
AH80

**5e. TASK NUMBER**

**5f. WORK UNIT NUMBER**

**7. PERFORMING ORGANIZATION NAME(S) AND ADDRESS(ES)**
US Army Research Laboratory
ATTN: RDRL-WMP-C
Aberdeen Proving Ground, MD 21005-5066

**8. PERFORMING ORGANIZATION REPORT NUMBER**
ARL-TR-8420

**9. SPONSORING/MONITORING AGENCY NAME(S) AND ADDRESS(ES)**

**10. SPONSOR/MONITOR'S ACRONYM(S)**

**11. SPONSOR/MONITOR'S REPORT NUMBER(S)**

**12. DISTRIBUTION/AVAILABILITY STATEMENT**
Approved for public release; distribution is unlimited.

**13. SUPPLEMENTARY NOTES**
primary author's email: <richard.c.becker.civ@mail.mil>.

**14. ABSTRACT**
The peak tensile stress at the spall plane in simulations explicitly modeling the growth and coalescence of voids from a random population of void nucleating particles is compared with the spall stress inferred from free surface velocity measurements. For square pulse loadings where the tensile stress exceeded the stress to initiate void growth, the peak tensile stress achieved at the spall plane dropped quickly and did not propagate outside of the spall process zone. The transient peak stress is reduced before the wave propagates. The remaining stress pulse that does leave the spall process zone propagates to the free surface with the expected degradation with propagation distance. Additional simulations on brittle materials also show that, for specimens loaded well above the spall stress, the peak stress can be released too quickly for it to propagate outside of the spall zone, and that the stress pulse received at the free surface may not reflect the peak stress at the spall plane.

**15. SUBJECT TERMS**
spall, velocimetry, fracture, visar

| 16. SECURITY CLASSIFICATION OF: | | | 17. LIMITATION OF ABSTRACT | 18. NUMBER OF PAGES | 19a. NAME OF RESPONSIBLE PERSON |
|---|---|---|---|---|---|
| a. REPORT | b. ABSTRACT | c. THIS PAGE | | | Richard Becker |
| Unclassified | Unclassified | Unclassified | UU | 29 | 19b. TELEPHONE NUMBER (Include area code) 410-278-7980 |

## Contents

## List of Figures

## 1. Introduction

Materials subjected to high impulsive loads can fail by spall where interaction of pressure release waves creates a tensile stress in excess of the material strength. The spall strength of a material can be inferred from several experimental techniques. In the most direct method, the applied loading is varied systematically, and recovered specimens are examined for spall damage. This involves some subjectivity to define the spall threshold, and many specimens are needed to obtain narrow bounds on the spall strength. A more common method to estimate spall strength relies on the peak tensile stress prior to spall failure being transmitted to the free surface. The peak stress is inferred from the magnitude of the velocity pull-back associated with the tensile stress. Several methods have been proposed for correcting this measurement for wave decay during transit to the free surface.[1] These typically depend on the spall stress pulse characteristics and wave speeds ahead of and behind the pulse.

A recent observation from a detailed simulation of void growth to coalescence at high stress levels[2] suggested that the inertia from the rapid void growth within the spall process zone reduced the peak stress level before it could propagate. As a result, the stress transmitted to the free surface was substantially less than the maximum tensile stress during the spall process. The implication is that the spall stress inferred from free surface velocity measurements of significantly overdriven specimens may not reflect the true spall strength. The purpose of this study is to examine the transmission of the peak stress to the free surface for a range of loading magnitudes to provide experimental guidelines.

## 2. Micro-Mechanical Model for Ductile Spall

### 2.1 Model Geometry

The configuration for the ductile spall simulations is a 0.1- $\times$ 0.1-mm section of a 2-mm-thick copper disk, shown in Fig. 1, similar to that used in Callaghan and Becker.[2] The volume contains 4775 spherical void nucleating particles, 2-$\mu$m diameter, yielding a 0.1% particle volume fraction. These were randomly placed within the model region with a minimum center-to-center separation distance of 14.4 $\mu$m. A sample of the distribution is shown in Fig. 2a. The volume was discretized with regular hexahedral elements, 0.5 $\mu$m on a side, for a total of 160 million elements. The resulting discretization of the initial particles is shown in Fig. 2b.

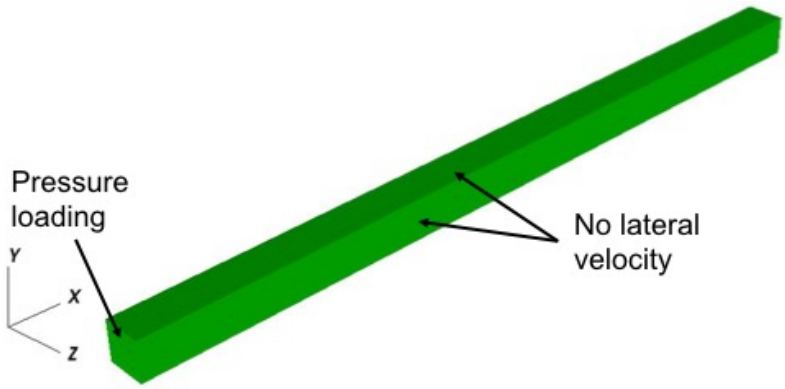


**Fig. 1 Model region for spall simulations. Pressure pulse loading is applied to the left surface.**

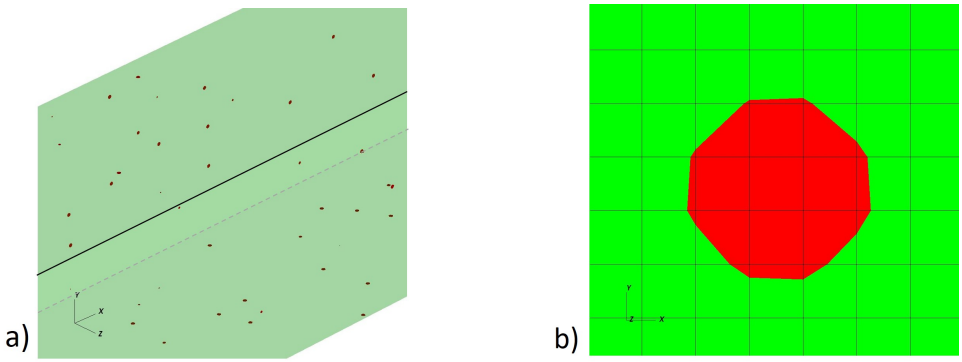


**Fig. 2 Zoomed-in views of a) particle distribution and b) mesh resolution of particles**

The lateral surfaces of the model region, shown in Fig. 1, are shear free and constrained from lateral motion to simulate uniaxial strain conditions associated with plate impact experiments. A pressure pulse loading is applied to the left end of the sample and the right end is free. The pressure loading was ramped from zero at a rate of 500 GPa/$\mu$s to peak pressures of 1, 1.5, 2, 3, 5, 10, 15, 20, and 30 GPa. The peak is held for approximately 0.5 $\mu$s and then released over a single time step. Since the shock transit time depends on peak pressure, due to pressure-dependent sound speed, a small adjustment of pulse duration is used to keep the spall plane acting over the same set of voids for all of the loadings.

## 2.2 Material Model Parameters

The flow strength of the target material, $\bar{\sigma}$, is described by a rate-independent J2-Flow Theory model with a Steinberg–Guinan strain-hardening relation.[3]

$$\bar{\sigma} = \sigma_0 \left[1 + \beta\, \varepsilon^p\right]^n \frac{G}{G_0} \quad , \tag{1}$$

where $\varepsilon^p$ is the equivalent plastic strain, $\sigma_0$ = 120 MPa is the initial flow strength, and $\beta$ = 36 and $n$ = 0.45 are strain-hardening parameters. A 640-MPa cap is placed on the flow stress to prevent excessive hardening. The flow stress is scaled by the ratio of the shear modulus, $G$, to its reference value, $G_0$:

$$G = G_0 \left[1 + bp - cT\right] \quad , \tag{2}$$

where $G_0$ = 47.7 GPa, and the pressure and temperature dependence are given by $b$ = 2.83×10$^{-5}$ MPa$^{-1}$ and $c$ = 3.77×10$^{-4}$ K$^{-1}$.

The equation of state (EOS) is modeled by the Mie–Grüneisen relation

$$p = \begin{cases} \frac{\rho_0 c_b^2 \mu \left[1 + \left(1 - \frac{\gamma_0}{2}\right)\mu - \frac{a}{2}\mu^2\right]}{\left[1 - (S_1 - 1)\mu\right]^2} + \left(\gamma_0 + a\mu\right) E & \text{if} \mu > 0 \\ \rho c_b^2 \mu + \left(\gamma_0 + a\mu\right) E & \text{otherwise} \end{cases} . \tag{3}$$

Here

$$\mu = \left(\frac{\rho}{\rho_0} - 1\right) \tag{4}$$

is the compression, and $E$ is the internal energy per unit reference volume. In the EOS, $\rho$ is the current density; $\rho_0$ = 8.93 g/cm$^3$ is the initial density; $c_b$ = 3940 m/s is the bulk sound speed; $S_1$ = 1.489 is the slope of the particle speed-sound speed curve; $\gamma_0$ = 2.02 is the Grüneisen parameter; and $a = 0.47$ is its density dependence. No failure model is prescribed for the matrix material.

The particles have the same flow strength and EOS as the matrix. The distinction is the activation of a failure criterion at a 10-MPa tensile pressure in the particles. This criterion is intended to model particle decohesion or particle fracture at very low stress levels. The stress is sufficiently small that its exact value is inconsequential for the range of applied loads. Void material is inserted into failed particles where the density falls below 95% of the reference density. The void material expands freely. This prevents unrealistically low densities of the particle material.

### 2.3 Numerical Treatment

The simulations are run in an arbitrary Lagrange–Eulerian (ALE) finite-element framework[4] where material flows through the evolving mesh. The mesh is positioned by an equipotential algorithm that moves the mesh with the external boundaries and keeps all of the interior elements roughly hexahedral and of the same size. Elements can contain multiple materials, and the advection algorithm accounts for movement of material volume fractions and material state from one element to another. The boundaries of the voids generated from the failed particles flow through the mesh as the pores grow, allowing the void growth to be captured explicitly.

Plots are created for velocities and state variables on the z-mid-plane cross section. In addition, the cross-section data are reduced by averaging the longitudinal stress over 20-$\mu$m windows along the length of the sample. The window provides average values over a volume spanning approximately 40 longitudinal elements, and its length is about 50% greater than the minimum particle spacing. Finally, velocity at a node on the specimen-free surface is recorded to emulate velocimetry data from experiments.

## 3. Results

### 3.1 Incipient Spall Evolution at 1.0 GPa

The longitudinal velocity field at 1.0 $\mu$s is presented in Fig. 3 for simulations with a 1.0-GPa loading pressure. At this time the wave from the tensile stress associated with the spall has traversed to the free surface on the right side of the specimen and has reflected. Incipient spall is evident from the open voids in the enlarged portion, but the loading was not sufficient for complete spallation. The near discontinuities in the velocity field indicate regions of intense plastic deformation, as observed in earlier studies.[2,5]

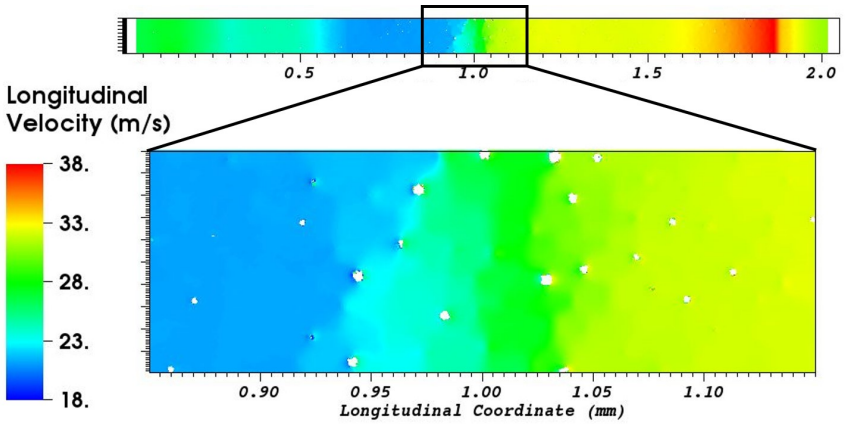


**Fig. 3 Overall and zoomed velocity field for 1.0-GPa pulsed loading at 1.0 $\mu$s showing void growth and localized deformation**

The stress evolution averaged over 20-$\mu$m slices near the spall plane is depicted in Fig. 4a. At the first time recorded, 0.748 $\mu$s, the release waves from the surfaces are partially overlapped. The portion of the release waves associated with the elastic-plastic transition have intersected, but the plastic waves have not yet interacted. This creates the initial stress plateaus at around 420 MPa while the stress at the center is still compressive. By 8 ns later, the main part of the release waves are interacting, and the peak tensile stress is above the plateau associated with the elastic-plastic transition. The peak continues to rise over time and then drops a bit to a fairly steady value of about 680 MPa by 0.840 $\mu$s. The stress at the center decreases a bit further as the simulation proceeds, but only to 600 MPa by 1.0 $\mu$s. During this process, the stress waves also propagate away from the center toward the surfaces. The slope and shape of the curve below the plateau tend to remain fairly consistent during propagation, but the slope of the portion above the plateau tends to decrease as the wave propagates.

The shape of the right-moving wave as it approaches the free surface at later times is shown in Fig. 4b. Both plots are to the same scale to facilitate comparison. As described previously, the lower portion of the front is fairly similar to that at earlier times in Fig. 4a, but the slope of the upper portion has changed considerably and the peak has dropped to about 640 MPa. Figure 4b also shows little stress drop at the center, as the stress at the left side of Fig. 4b is approximately constant for the 20-ns time interval. This is consistent with incipient spall at the 1.0-GPa loading.

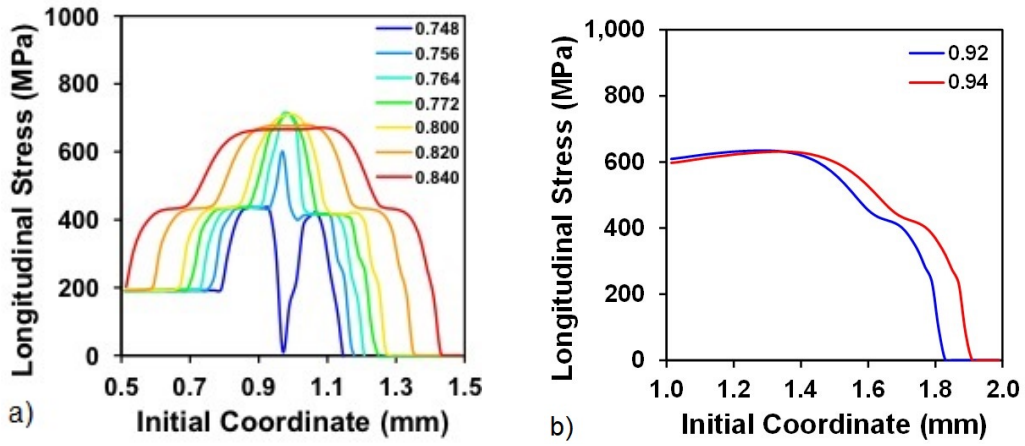


**Fig. 4 Longitudinal stress for 1-GPa loading pulse averaged over 20-$\mu$m windows at a) the center of the specimen and b) near the free surface. The numbers on the plot legends depict the times in microseconds. Both plots are to the same scale.**

## 3.2 Complete Spall at 1.5-GPa Loading

Similar results are obtained for the 1.5-GPa pressure loading, except that the higher loading impulse was sufficient to cause complete spall at 1.0 $\mu$s (Fig. 5). The velocity discontinuity is abrupt, as would be expected with complete fracture.

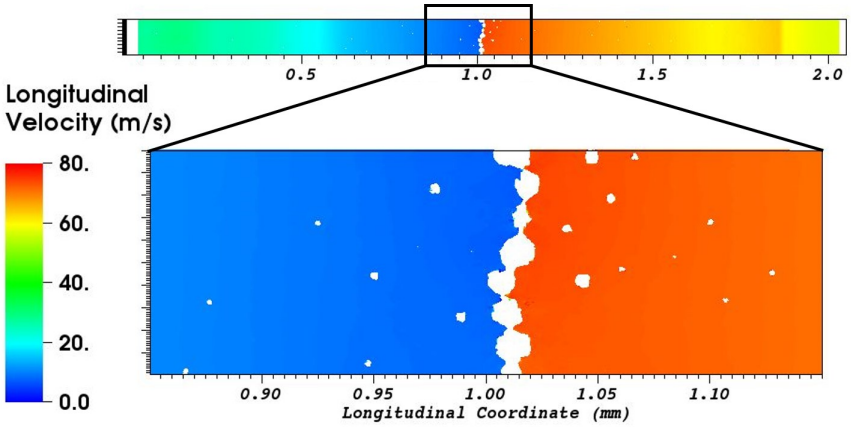


**Fig. 5 Overall and zoomed velocity field for 1.5-GPa pulsed loading at 1.0 $\mu$s showing voids coalesced to form the failure surface**

The evolving stress profile near the center of the specimen is shown in Fig. 6a. At 0.748 $\mu$s, prior to the interaction of the plastic release waves, the stress at the center is still compressive. As with the 1.0-MPa loading, the waves ahead of the elastic-plastic transition interact to create a plateau at around 425 MPa. By 0.756 $\mu$s the main release waves have interacted, and the tensile stress hits 1.0 GPa. The stress at

the center subsequently falls, but the waves are propagating away from the center at the same time, which results in traveling peaks at both sides of a center dip, as is shown by the 0.764-$\mu$s curve. The stress at the center continues to drop, and for the next 8 ns, the release rapidly consumes the side peaks before they can propagate outside of the process zone. The rate of stress reduction at the center then decreases, and the remaining waves propagate while the stress at the center is slowly reduced.

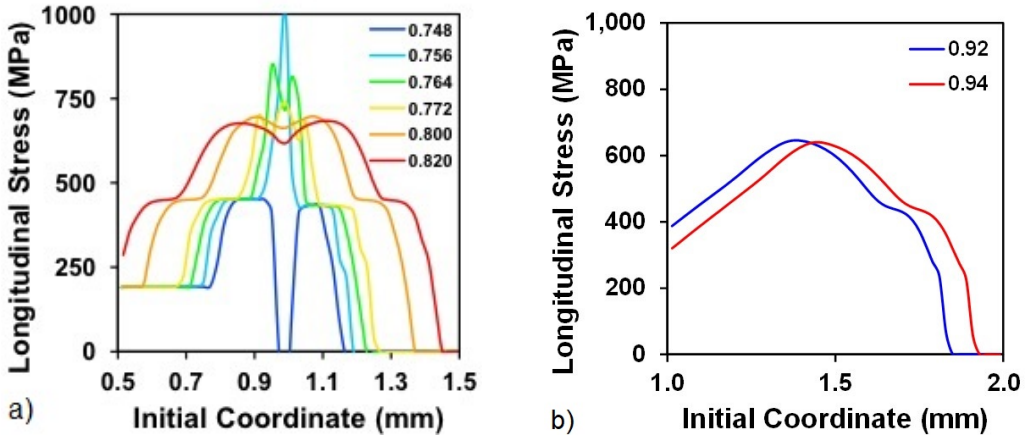


**Fig. 6 Longitudinal stress for 1.5-GPa loading pulse averaged over 20-$\mu$m windows at a) the center of the specimen and b) near the free surface. The numbers on the plot legends depict the times in microseconds. Both plots are to the same scale.**

As with the 1.0-GPa simulations, there is a plateau associated with the elastic-plastic transition. The portion of the curve below this plateau propagates toward the surface with little change, and the slope of the leading front above the plateau decreases with time and propagation distance, as shown in Fig. 6b. The stress at the center, the left side of Fig. 6b, also continues to decrease with time as the spall surface is forming.

An additional feature from Fig. 6b, which is not noticeable in Fig. 4b, is the erosion of the peak stress. This erosion is a result of the trailing edge of the wave running faster than the leading edge. This is a well-known phenomena (see, e.g., Antoun et al.[1]) where the trailing edge is associated with elastic processes and moves at the longitudinal wave speed, and the leading edge, particularly above the plateau, is associated with plastic processes and moves at a lower speed. In the plots, this is evidenced by the horizontal spacing between the curves being greater on the trailing slope than on the leading slope, particularly the leading plastic slope above the plateau.

### 3.3 Stress Evolution at Higher Loading

The stress evolution at the center of the model regions is depicted at progressively higher applied pressures in Fig. 7. The width of the applied stress pulse is adjusted slightly to maintain the peak stress at the middle of the model region as the wave speed increases with higher pressures. The important feature of all these plots is that the peak tensile stress is well in excess of the tensile stress that propagates to the surface. For loading pressures 5 GPa (Fig. 7c) and above, the longitudinal stress goes through a compressive transient as spallation progresses, as noted by Callaghan and Becker[2] and described in the next section. The peaks remaining to the sides of the plummeting central valley, and inboard of the elastic-plastic plateau, diminish steadily as the trailing edge of the wave propagates faster than the leading edge. These are most evident at the lower stress levels in Fig. 7.

For applied pressures up to 5 GPa, Fig. 7c, the maximum tensile stress rises with loading pressure and peaks at the center of the specimen. For loading pressures of 10 GPa and above, the maximum tensile stress tends to plateau at the center of the specimen. The magnitude increases slowly with increased pressure, and the width of the central plateau also increases. It is important to note that the stress level in the shoulder plateau area of the plots, outside of the central portion, also increases with increased loading pressure. This is due to a combination of strain hardening, as the plastic strain increases with loading pressure, and the pressure dependence of the flow stress shown in Eq. 1 and Eq. 2.

The peak tensile stress and the stress from the elastic-plastic plateau are plotted, respectively, as the blue and red curves in Fig. 8. The green curve is the longitudinal stress near the exit, before the magnitude is reduced by the free surface reflections. This green curve is indicative of the stress that would be measured by free surface velocimetry.

The peak stress increases rapidly with loading pressure and then levels off after about 5 GPa. This feature is coincident with the broadening of the central plateau in Fig. 7d and later. The mechanism for the peak stress appearing to level off has not been pursued. It could be due to maxing out the inertial over-stress sustainable by the configuration, or it could be related to the void spacing and wave propagation rate.

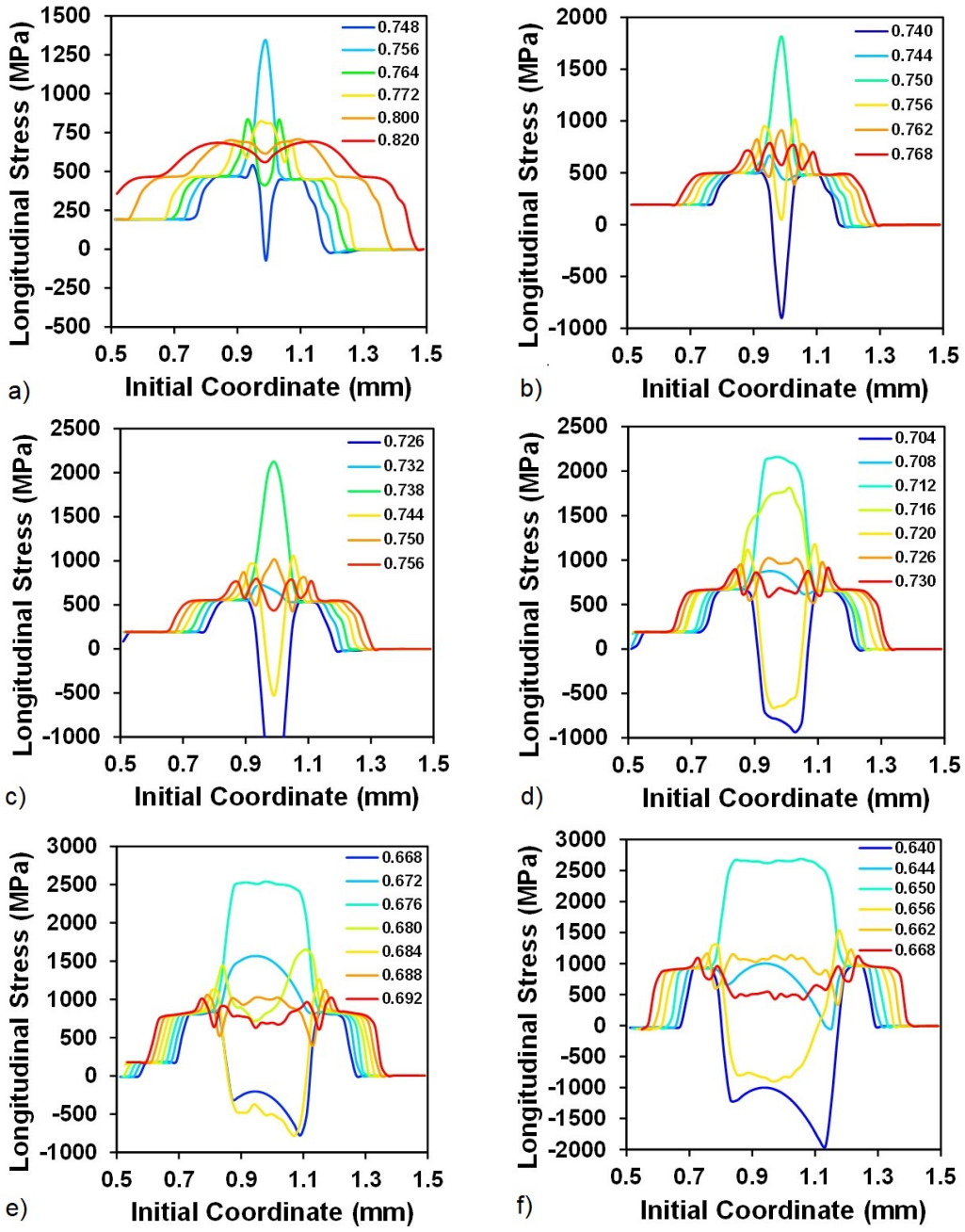


**Fig. 7 Longitudinal stress history averaged over 20-$\mu$m windows at the center of the specimen for peak loading of a) 2 GPa, b) 3 GPa, c) 5 GPa, d) 10 GPa, e) 20 GPa, and f) 30 GPa. The numbers on the legends depict the times in microseconds. The subplots are on different y-axis scales.**

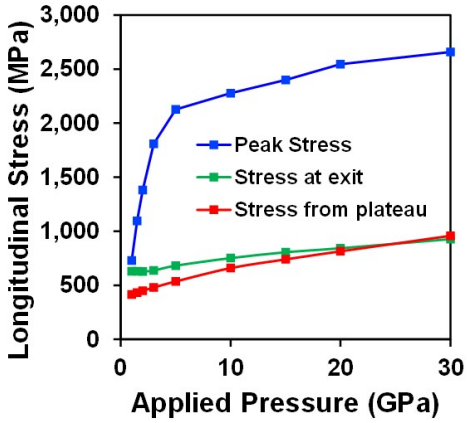


**Fig. 8 Longitudinal stress as a function of loading pressure at its peak value, near the exit before free surface reduction, and at the elastic-plastic plateau**

An expression for the longitudinal stress change at the elastic-plastic plateau can be obtained for low loading pressures where the moduli are approximately constant. In the dispersive release wave reflected from the free surface, the plateau stress is approximately

$$\sigma_{xx} \simeq 2\bar{\sigma}\left(\frac{\kappa}{2G}+\frac{2}{3}\right) \quad , \tag{5}$$

where $\kappa$ is the bulk modulus and $G$ is the shear modulus. This is twice the stress at the Hugoniot elastic limit as it accounts for unloading from the full shock loaded state and reloading in tension to the elastic-plastic limit. When the left and right traveling waves meet at the center, the pressure part of the waves combine as elastic waves to give a pressure within the plateau of $p = \bar{\sigma}\kappa/G$, but plastic flow intervenes for the deviatoric part. The resulting elastic-plastic plateau stress propagating to the free surfaces is approximately

$$\sigma_{xx} \simeq \bar{\sigma}\left(\frac{\kappa}{G}+\frac{2}{3}\right) \quad . \tag{6}$$

Strain hardening and property dependence of the moduli and the flow strength on pressure at higher loadings add a complex history dependence to Eq. 6 and raise the level of the plateau, as seen in Fig. 8.

A 1-D simulation of a homogeneous material with a fixed spall strength was run using the 10-GPa pressure boundary condition. The simulation used the same constitutive model as the matrix material but with 2.5-GPA spall strength imposed. Figure 9a shows the longitudinal stress profile for the model with the simple spall

criterion and the detailed model (curve from Fig. 7d) at 0.730 $\mu$s. The 1-D model is given by the red curve. It can be seen that wave timing is the same for the two runs and that the stress plateau levels are similar. The zero stress in failed particles is largely responsible for the plateau stress level being lower in the large-scale run, and averaging the stress over 20-$\mu$m slices smooths the corners of the stress profile. When using the prescribed spall model, the stress immediately drops to zero when the spall stress is reached. A 0.2-$\mu$m portion of the model reaches this stress, as indicated by the wide trough. The stress in the detailed model decays more slowly since it is tied to void growth processes.

At 0.890 $\mu$s, Fig. 9b, the tensile waves for the two simulations have reached the free surface. The leading edges are still coincident, but the faster-moving trailing wave has eaten away much of the pulse width for the 1-D simulation with abrupt failure. The gradual stress reduction in the detailed simulation provides support for the trailing edge, which reduces the erosion rate. Overall, the similarity of the wave locations and plateau height between the two solutions demonstrates that the plateau is related to the material flow strength and not the porosity or failure progression.

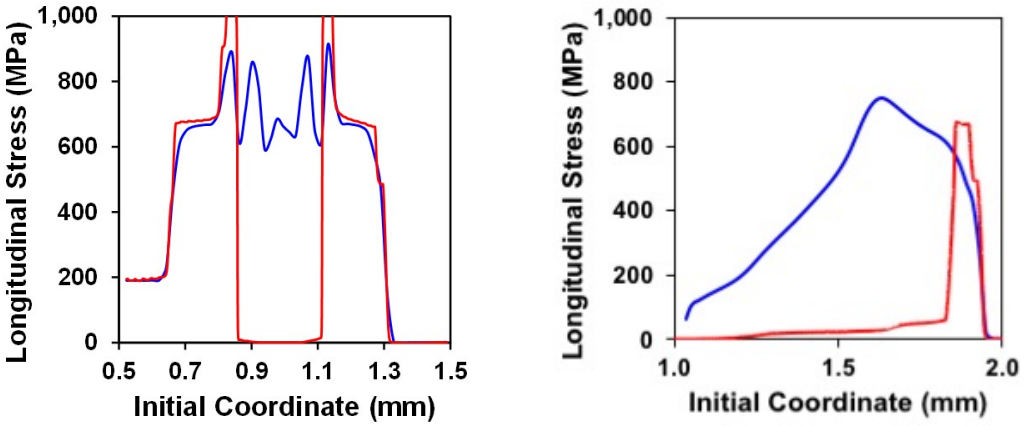


**Fig. 9 Longitudinal stress for a 10-GPa pulse loading applied to the full model and to a 1-D model using a threshold spall criterion of 1.5 GPa at a) 0.730 $\mu$s and b) 0.890 $\mu$s. The blue curves are for the detailed model, and the red curves are for the simulation with an abrupt failure model.**

### 3.4 Free Surface Velocity Correlation

The spall strength of a material is typically inferred from an experimentally measured free surface velocity profile. The velocity time history recorded for the simulations is plotted in Fig. 10 for applied pressure loadings up to 10 GPa.

The short dashed curve segments in Fig. 10 are created by transmuting the longitudinal stress profile as it nears the free surface (e.g., in Fig. 4b) into velocity using

$$v = v_x - \sigma_{xx} \frac{c_l + c_b}{\rho \, c_l \, c_b} \quad , \tag{7}$$

where $v_x$ is the steady free surface velocity prior to pullback; $\sigma_{xx}$ is the longitudinal stress at some location, $x$; $\rho_0$ is the reference density; and $c_l$ and $c_b$ are the longitudinal and bulk sound speeds, respectively. The $x$-coordinate associated with the longitudinal stress data is converted to time using the bulk sound speed and a time offset.

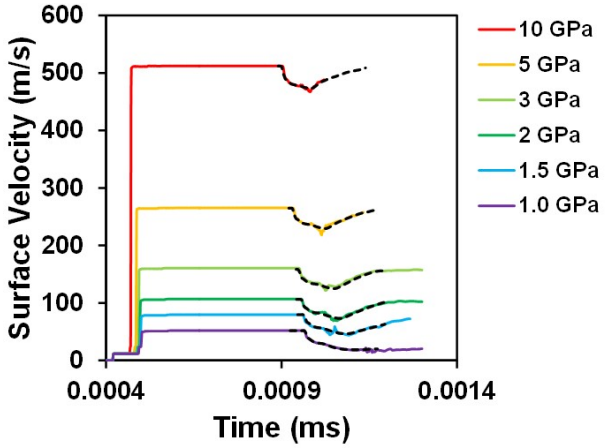


**Fig. 10 Free surface velocity plotted with velocity obtained by transmuting the longitudinal stress profile near the exit**

The recorded velocities are measurements at a point (a finite-element node), whereas the converted stress is from an average over a volume. Hence, the transmuted stress would be expected to produce a smoother curve. With this consideration, the dashed lines from the transmuted stress follow the free surface velocity fairly closely except for short transients in a few of the velocities. The agreement confirms that experimental velocimetry provides an accurate representation of the stress near the free surface. The uncertainty is in how closely the stress profile propagating to the surface reflects the peak stress at the spall plane.

### 3.5 Inertial Effects

Callaghan and Becker[2] determined that the brief compressive stress at higher loading pressures is associated with an inertial overshoot related to the rapid void growth. This effect is revisited here for the 10-GPa loading.

Figure 11 shows results from the 10-GPa loading simulation at 0.712 $\mu$s and 0.720 $\mu$s. These times correspond, respectively, to the peak tensile stress in Fig. 7d and the subsequent lowest compressive stress. The longitudinal stress plotted in Fig. 11a shows that most of the central portion of the specimen is near 2500 MPa, and it is interspersed with spheroids of reduced stress around the voids. The stress rose rapidly, and the release from the free surfaces of the voids has not yet had time to propagate far. By 8 ns later, Fig. 11b, the mean stress level at the center is substantially compressive with regions of zero stress around the voids, in agreement with the corresponding curve in Fig. 7d. In the transient between these two states, the stress is released around the voids, beginning from the void surfaces. The release initiates within the specimen volume. It is distributed, not propagated from a point or plane. This mechanism allows the tensile stress to be released very rapidly, before it has the opportunity to propagate outside of the spall process zone. The peak stress at 0.726 $\mu$s in Fig. 7d is significantly less than the peak at earlier times.

The mechanism creating the compressive stress is elucidated by examining the velocity fields in Figs. 11c and 11d. The important feature to note is that the right-hand void surfaces are moving faster to the right than the bulk material at that longitudinal location; and, similarly, the left-hand void surfaces are moving faster to the left than the bulk material at any location. This indicates that the voids are expanding faster than the mean strain rate from before 0.712 $\mu$s to after 0.720 $\mu$s. Since the void expansion rate is faster than the mean over more than a 8-ns time period, it puts the material in compression. However, void expansion in a compressive stress field is not consistent with static equilibrium, so it must be driven by the void growth dynamics. The inertia of the rapid void growth creates the compressive state. This was noted in the analytic solution of Wright and Ramesh.[6]

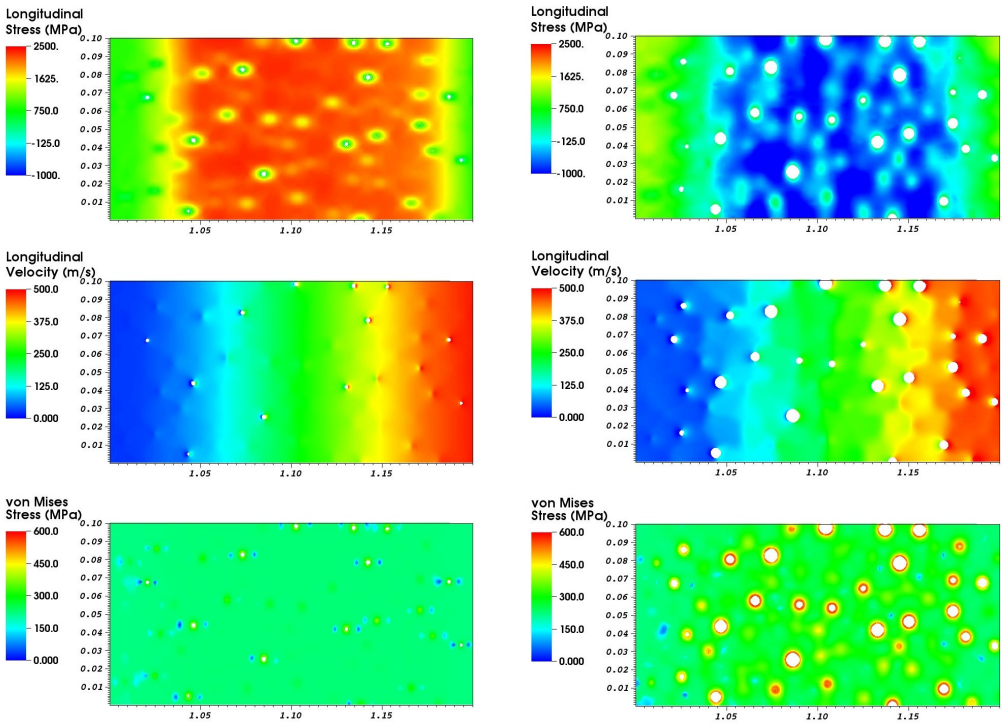


**Fig. 11 Fields from the 10-GPa loading simulation at 0.712 $\mu$s (left column) and at 0.720 $\mu$s (right column). Plots are of longitudinal stress, a) and b); longitudinal velocity, c) and d); and von Mises effective stress, e) and f).**

The von Mises stress effective at 0.712 $\mu$s and 0.720 $\mu$s is plotted in Figs. 11d and 11e, respectively. The initial yield strength is 120 MPa, and strain hardening during the shock compression and release raises the effective stress level nearly uniformly. Void growth, on the other hand, involves considerable strain at the void surfaces, and a commensurate increase in the equivalent stress around the voids due to strain hardening is seen at 0.720 $\mu$s. Thermal softening proportional to the shear modulus reduction is included in these simulations, but it is overwhelmed by the strain hardening.

## 3.6 Effects of Rate Dependence

The simulations described previously used a rate-independent material model. However, it is known that the strain rate at the void surfaces can be very high and that strain rate effects can increase the stress substantially (e.g., Wilkerson and Ramesh[7]). The Preston–Tonks–Wallace[8] (PTW) model was used to examine the effects of strain rate dependence. It includes enhanced rate sensitivity at high strain rates to simulate effects of phonon drag. The equations and parameters are given in

the original PTW paper, with the pressure- and temperature-dependent shear modulus given by Eq. 2.

Results from the simulation with the PTW model at 10-GPa loading are shown in Fig. 12. The times selected correspond to the peak longitudinal tensile stress and the lowest stress immediately subsequent to the peak. These are 0.720 $\mu$s and 0.728 $\mu$s, respectively, which are a bit later than the rate-independent solution shown in the previous section. The rate dependence leads to higher stresses, which delays void growth. In comparing the two sets of results, it is notable that the peak stress is significantly higher because of the strain rate sensitivity and that subsequent lowest longitudinal stress is tensile rather than compressive. In the rate-independent case, the stress is reduced approximately 2700 MPa in the 8 ns between the plot sets, and with the rate-dependent solution, the stress reduction is about 2000 MPa over the same time interval. Hence, the positive stress in Fig. 12b compared to Fig. 11b is due to at least two factors. First is the higher peak stress from which the reduction starts, and the second is a lesser stress reduction. The lower stress reduction is related to less void growth in the intervening 8 ns for the rate-dependent material. This can be seen by comparing the two time states (i.e., plots a to b) for the two strength models. The PTW model simulation shows larger voids than the rate-independent solution at the start of the interval and smaller voids at the end of the 8-ns interval.

As with the rate-independent material model, Figs. 12c and 12d show that the void growth is more rapid than the mean strain rate. But while the void growth rate is more rapid than the mean expansion, the void growth inertia is not sufficient, compared to the dissipative mechanisms, to drive the stress into compression. The void growth rate is slower, as noted above. The flow strength governing the plastic dissipation is shown by the von Mises effective stress plots in Figs. 12e and 12f. The peak effective stress levels around the voids at 0.720 $\mu$s are significantly higher than the mean strength, and the volume of material at elevated strength in the regions of sharp strain gradients is even greater at the later time. Due to these higher stress levels, the dissipated energy is substantially greater with the rate-dependent model.

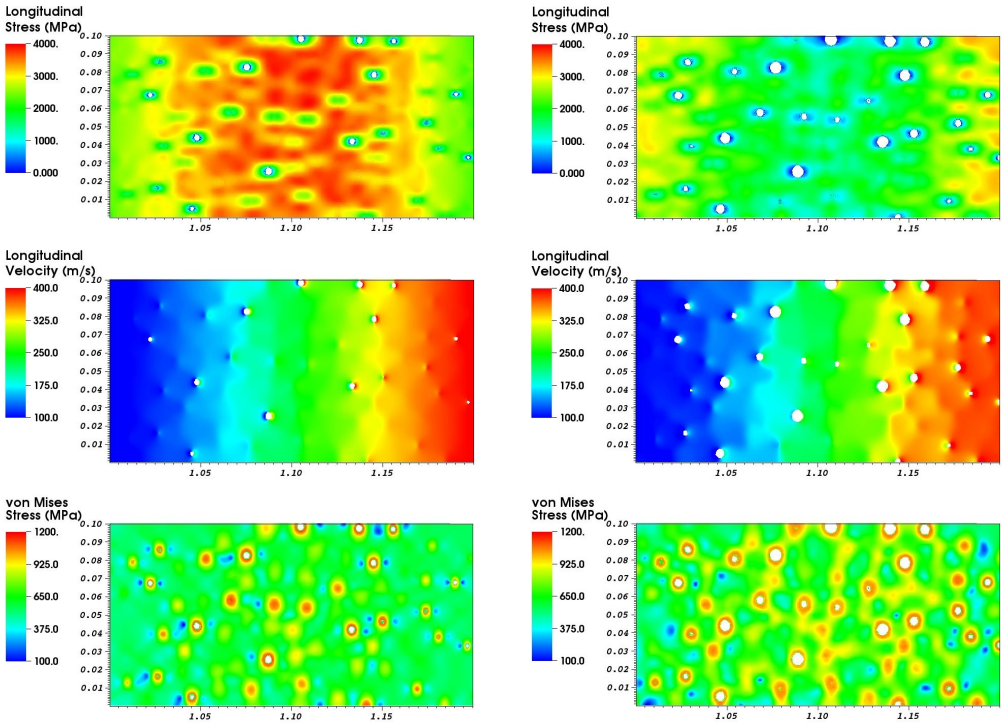


**Fig. 12 Fields from the simulation with the PTW model and the 10-GPa loading at 0.720 $\mu$s (left column) and at 0.728 $\mu$s (right column). Plots are of longitudinal stress, a) and b); longitudinal velocity, c) and d); and von Mises effective stress, e) and f).**

The averaged longitudinal stress profile at the center during spall, and later near the free surface, is shown in Fig. 13 for the PTW model. In contrast to the rate-independent solution, there are no distinct elastic-plastic plateaus. Similar to the rate-independent simulations, the peak stress at the center is reduced substantially in the 8 ns following the peak (Fig. 13a). The decrease by 0.728 $\mu$s is about 2000 MPa at the center and less to the sides of the trough. Over the next 0.022 $\mu$s the longitudinal stress at the center remains roughly constant, while the side peaks propagate and decrease. With the combined propagation and side peak reduction, the slope of the back side of the propagating wave is substantially diminished.

As the stress profile propagates to the surface in the next 0.1 $\mu$s, both the plastic slope on the wavefront and the slope on the backside of the wave continue to decrease (Fig. 13b). The stress at the spall plane drops to a few 100 MPa in this time as the void growth continues. Consequently, the highest stress arriving at the surface is approximately 1500 MPa less than the true peak stress. Hence, while accounting for strain rate sensitivity with the PTW model may lessen the stress drop in the

spall process zone, it does not modify the rapid expansion of the voids sufficiently to prevent a substantial stress reduction.

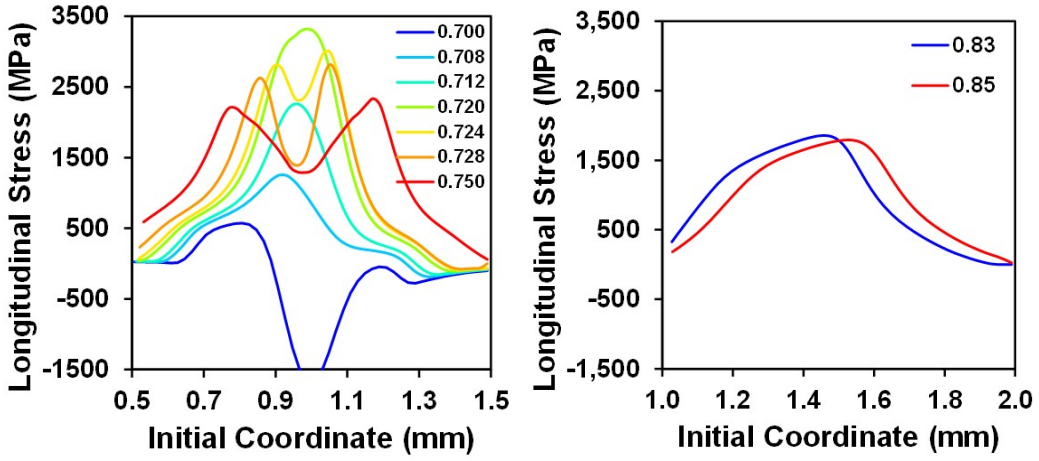


**Fig. 13 Longitudinal stress distribution for the 10-GPa loading with the PTW model at a) the center of the specimen during the spall event and b) near the free surface as the wave arrives**

## 3.7 Inferred Spall Stress for Brittle Materials

The reduction of the peak stress before it leaves the process zone for ductile spallation raises the question of whether a similar stress reduction occurs in brittle materials. While brittle materials are not the focus of this report, a limited series of simulations was run to explore the possibility. Unlike the void growth analyses reported previously, it is not possible to resolve the details of the brittle failure process in a full-scale simulation. The brittle fracture is simulated by a recently developed constitutive model,[9] with the failure stress in tension being approximately 570 MPa. The reader is referred to the report by Tonge[9] for all of the equations and parameters. The simulations were 1-D uniaxial strain, and they were run at 1-, 2-, 3-, and 5-GPa loading pressures. The duration of the pressure pulse was adjusted to initiate the spall near the center of the sample.

The results are presented in Fig. 14. The time evolution of the stress profile for the 5-GPa run is shown in Fig. 14a. At 0.216 $\mu$s the material is still undamaged. The release waves have begun to interact, but the stress at the center of the specimen is still compressive. By 1 ns later, most of the center millimeter of the specimen is in tension at the failure stress, and there is a downward blip where failure has already occurred. By 0.218 $\mu$s, the constitutive model has dropped the stress to zero for all material that exceeded the spall strength. There is an oscillation at the left

side of the failure process zone originating from the failure blip that was evident 1 ns earlier. The bump to the right of center for the 0.218-$\mu$s curve indicates a region of unfailed material. This stress pulse will propagate to the right. At 0.219 $\mu$s the tensile stress at the fractured interface has snapped back, providing a small compressive component to the red curve. The waveform continues to evolve as it propagates to the free surface on the right, with the peak continuously decreasing.

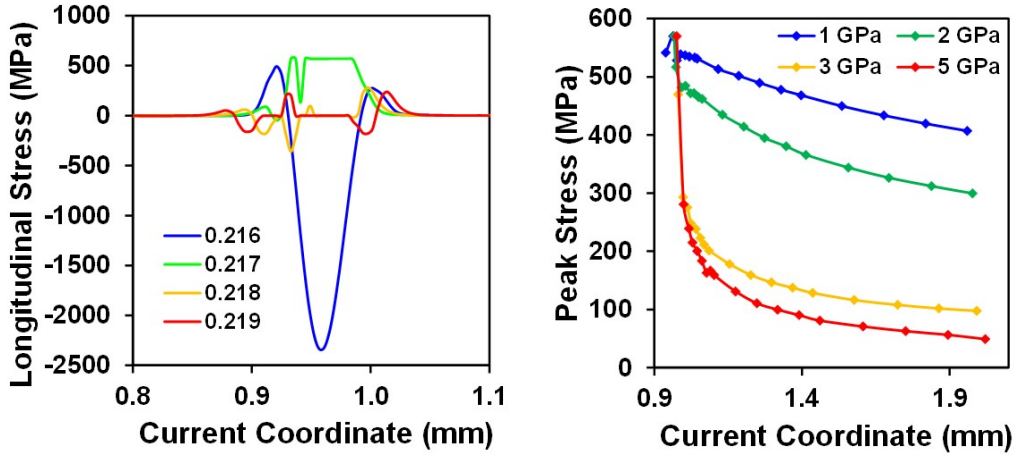


**Fig. 14 Results from brittle failure model: a) stress profile at several times (in microseconds) near the spall time for the 5-GPa pulse loading and b) the peak stress tracked through time as the stress pulse runs to the surface**

The time evolution of the peak tensile stress for this and the other applied loadings is given in Fig. 14b. All show the tensile peak at the 570-MPa spall strength set by the constitutive model. The red curve for the 5-GPa loading confirms the sharp initial drop followed by a gradual decline described previously. The results at the lower applied pressures have a less severe initial decrease, but the gradual decline with propagation is common for all. As with the ductile spall results, the peak stress pulse is severely curtailed before it leaves the spall zone for loadings with high overstress. There is no initial stress drop for loadings near the spall threshold. The peak decays with distance propagated for all loading pressures.

## 4. Summary and Conclusions

Detailed numerical simulations of void growth and coalescence for ductile spall demonstrate that the peak tensile stress generated in an overdriven spall experiment can be substantially reduced before the stress pulse leaves the spall process zone. The stress reduction spreads from the multiple voids within the volume, which fa-

cilitates the rapid stress release within the process zone. Inertial effects can further modify the stress history by raising the stress required to initiate void growth and then sustaining void growth to undershoot the equilibrium stress field. The loss of the peak stress before it leaves the spall process zone confounds experimental measurement of spall strength.

Both the stress reduction and the inertia effects can be largely suppressed by conducting the experiments at loading levels creating incipient spall. The longitudinal stress at incipient spall evolves slowly, so there is no substantial stress release and there is minimal void growth inertia. In addition, the stress wave running to the surface is supported by sustained tensile stress in the spall process zone so the peak stress changes little during propagation. The stress required for incipient ductile spall can be measured accurately with standard velocimetry techniques.

Inertia can contribute substantially to the longitudinal stress required to initiate void growth. Consequently, the incipient spall stress can be notably lower than the spall stress at high loading rates. Since the inertial stress contributions may not propagate beyond the process zone, their magnitude cannot be measured or even estimated from free surface measurements. The inertial effects must be inferred from models and included explicitly in models simulating spallation.

The spall stress in the process zone of brittle materials is also affected by overstress. For the limited cases examined, greater overstress creates a larger stress drop following brittle spallation. The peak stress is not transmitted outside of the spall process zone. As with ductile spall, the stress drop is minimized if the peak tensile stress is near the spall strength. After the initial drop, the remaining tensile stress peak decays as it propagates to the free surface. Placing the spall plane near the free surface or applying spall corrections will ameliorate the propagation losses. Both are standard approaches.[1]

## 5. References


1. Antoun T, Seaman L, Curran DR, Kanel GI, Razorenov SV, Utkin AV. Spall fracture. 1st ed. New York, USA: Springer-Verlag; 2003.

2. Callaghan K, Becker R. Examination of ductile spall failure through direct numerical simulation. In: Chau R, Germann TC, Lane JMD, editors. Shock Compression of Condensed Matter – 2017; Vol. 1979; 2018; St. Louis, MO. Melville (NY): American Institute of Physics; 2018. p. 070010.

3. Steinberg DJ, Cochran SG, Guinan MW. A constitutive model for metals applicable at high-strain rate. Journal of Applied Physics. 1980;51(3):1498-1504.

4. Nichols AL. ALE3D. An arbitrary Lagrange/Eulerian 2D and 3D code system. Livermore (CA): Lawrence Livermore National Laboratory; V4.28 ed. 2018. LLNL-SM-681737.

5. Becker R. Direct numerical simulation of ductile spall failure. Int. J. Fracture. 2017;208:5-26.

6. Wright TW, Ramesh KT. Dynamic void nucleation and growth in solids: A self-consistent theory. J. Mech. Phys. Solids. 2008;56:336-359.

7. Wilkerson JW, Ramesh KT. A closed-form criterion for dislocation emission in materials under arbitrary thermomechanical loading. J. Mech. Phys. Solids. 2016;86:94-116.

8. Preston DL, Tonks DL, Wallace DC. Model of plastic deformation for extreme loading conditions. J. App. Phys. 2003;93:211-220.

9. Tonge AL. Development of a ceramic material model for approximating the behavior of cracks within a continuum simulation framework. Aberdeen Proving Ground (MD): Army Research Laboratory (US); in press.

## List of Symbols, Abbreviations, and Acronyms

| | |
|---|---|
| 1-D | one-dimensional |
| ALE | arbitrary Lagrangian Eulerian |
| EOS | equation of state |
| PTW | Preston–Tonks–Wallace |

1 (PDF) DEFENSE TECHNICAL INFORMATION CTR DTIC OCA

2 (PDF) DIR ARL
IMAL HRA
RECORDS MGMT
RDRL DCL
TECH LIB

1 (PDF) GOVT PRINTG OFC
A MALHOTRA

ABERDEEN PROVING GROUND

17 (PDF) RDRL-WM
A RAWLETT
S SCHOENFELD
RDRL WMP B
C HOPPEL
T WEERASOORIYA
RDRL WMP C
R BECKER
D CASEM
J CLAYTON
R LEAVY
J LLOYD
C MEREDITH
S SATAPATHY
L SHANNAHAN
A TONGE
C WILLIAMS
RDRL WMM B
B LOVE
P MOY
T WALTER